THE JOURNAL OF PHYSICAL CHEMISTRY A
A JOURNAL OF THE AMERICAN CHEMICAL SOCIETY

pubs.acs.org/JPCA Article

Theoretical Study of the Atmospheric Chemistry of Methane Sulfonamide Initiated by OH Radicals and the $CH_3S(O)_2N^{\bullet}H$ + $^3O_2$ Reaction

Parandaman Arathala and Rabi A. Musah*

Cite This: J. Phys. Chem. A 2022, 126, 9447−9460 Read Online

ACCESS | Metrics & More | Article Recommendations | SI Supporting Information

Downloaded via UNIV ALBANY STATE UNIV NEW YORK on January 9, 2023 at 15:58:26 (UTC).
See https://pubs.acs.org/sharingguidelines for options on how to legitimately share published articles.

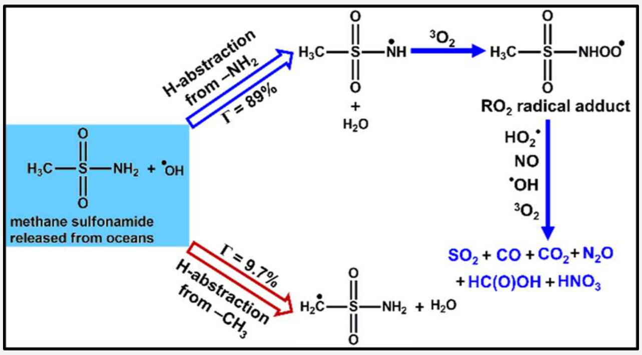

ABSTRACT: In the present work, we have revisited the reaction mechanism of the atmospheric oxidation of methane sulfonamide ($CH_3S(=O)_2NH_2$; MSAM) initiated by hydroxyl (OH) radicals in the gas phase. The present reaction has been studied for the first time using quantum calculations combined with chemical kinetic modeling. The abstraction of an H-atom from the $-NH_2$ group of MSAM by OH radical to form the products $CH_3S(=O)_2N^{\bullet}H$ + H_2O was found to be a major path with a barrier height of ~2.3 kcal mol^{-1} relative to the energy of the separated MSAM + $^{\bullet}OH$ starting reactants. This study is the first to identify the reaction of MSAM with $^{\bullet}OH$ as exclusively generating N-centered MSAM radicals. The chemical kinetic calculations for various paths associated with the MSAM + $^{\bullet}OH$ reaction were performed under pre-equilibrium approximation conditions using canonical variational transition state theory, employing the small curvature tunneling method in the temperature range of 200−400 K. A recent experimental study reported that OH radical-mediated degradation of MSAM proceeds via the formation of the C-centered MSAM radical ($^{\bullet}CH_2S(=O)_2NH_2$) product. However, the energetics and rate coefficient calculations in the present work suggest that the formation of the N-centered MSAM radical is a major path compared to that which proceeds via the C-centered MSAM radical. The overall rate coefficient for the MSAM + $^{\bullet}OH$ reaction was calculated in the 200−400 K temperature range. The overall rate coefficient for the MSAM + $^{\bullet}OH$ reaction was estimated to be $k = 1.2 \times 10^{-13}$ cm^3 $molecule^{-1}$ s^{-1} at 298 K. This rate coefficient at 298 K agrees well with the reported experimental value (1.4×10^{-13} cm^3 $molecule^{-1}$ s^{-1}) at the same temperature. We also provide branching ratios for each path associated with the MSAM + $^{\bullet}OH$ reaction. In addition, the atmospheric implications for the title reactions are discussed. The oxidation mechanism of the MSAM + $^{\bullet}OH$ reaction suggests that the formed $CH_3S(=O)_2N^{\bullet}H$ further reacts with atmospheric oxygen ($^3O_2$) to form the corresponding RO_2 radical adduct. The downstream products of the $CH_3S(=O)_2N^{\bullet}H$ + $^3O_2$ reaction in the present work indicate that sulfur dioxide (SO_2), carbon monoxide (CO), carbon dioxide (CO_2), nitric acid (HNO_3), nitrous oxide (N_2O), and formic acid [HC(O)OH] are formed as final products.

1. INTRODUCTION

Volatile organosulfur compounds (VOSCs) play an important role in the global sulfur cycle.[1] They are involved in important phenomena such as global warming, climate change, and acid precipitation.[1] Both natural processes and anthropogenic activities are responsible for the emission of OSCs into the atmosphere. In particular, oceans are the largest natural source of sulfur emissions, and they play a crucial role in the atmospheric chemistry of many trace compounds. OSC emissions from phytoplankton comprise up to 60% of the total sulfur flux into the marine boundary layer.[2−4] They act as a main source of the sulfate aerosols observed in remote oceanic areas and are responsible for the radiation balance at the earth's surface.[5,6] Dimethyl sulfide (DMS), an important natural sulfur source, is emitted from the oceans and accounts for almost half of the natural global atmospheric sulfur budget.[3] Other important sulfur compounds in the marine atmosphere include dimethyl sulfoxide, dimethyl sulfone, methyl sulfonic acid, and methyl sulfinic acid.[7] The fates of these compounds in their reactions with OH radicals have been reported, and their atmospheric lifetimes with respect to OH radicals are estimated to range from hours to several weeks.[8,9] In addition to the sulfur compounds, nitrogen-containing molecules are also present in ocean atmospheres. Various studies have

Received: September 8, 2022
Revised: October 24, 2022
Published: December 13, 2022

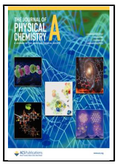

ACS Publications © 2022 American Chemical Society

https://doi.org/10.1021/acs.jpca.2c06432

reported that organic and inorganic forms of nitrogen, such as amines (R−NH_2), nitrous oxide (N_2O), and ammonia (NH_3), are emitted from highly biologically active upwelling regions of the oceans.[10−16] These studies reveal that sulfur- and nitrogen-containing trace compounds are present in ocean atmospheres and that they may strongly influence the global sulfur and nitrogen cycles.[1,17−19]

Edtbauer et al. recently reported the detection for the first time, of methane sulfonamide ($CH_3S(=O)_2NH_2$, MSAM) which contains both sulfur and nitrogen functionalities, in ambient air during the Air Quality and Climate Change in the Arabian Basin (AQABA-2017) campaign.[7] The concentration of MSAM was observed to be in the range of 20−50 parts per trillion (ppt), with a maximum value of ~60 ppt over the Arabian Sea. There are no reports on the potential sources of MSAM in the gas phase or in biological systems. Edtbauer et al. suggested that it may be formed from DMS via ocean-microbe-mediated activities that result in the emission of MSAM into the atmosphere.[7] This compound contains both S and N atoms in the form of a sulfonamide ($-S(=O)_2NH_2$) functional group, which is fairly common in various antibacterial drugs.[20] MSAM has also been detected in human urine.[21] This compound was not known to be an important atmospheric trace gas prior to the study of Edtbauer et al.[7] Recently, photo-oxidation in air of MSAM initiated by the OH radical was studied at 298 K and 700 Torr in a photochemical reactor, using Fourier transform infrared spectroscopy.[8] The rate coefficient for the reaction, determined using the relative rate technique, was $k = (1.4 \pm 0.3) \times 10^{-13}$ cm^3 $molecule^{-1}$ s^{-1} at 298 K. The major end products were reported to be carbon dioxide (CO_2), carbon monoxide (CO), sulfur dioxide (SO_2), and nitric acid (HNO_3). Formic acid (HC(O)OH) and N_2O were reported to be minor end products.[8] A reaction mechanism was proposed based on the results of numerical simulations and time-dependent formation of the end products. In summary, the results suggested that the MSAM + $^\bullet$OH reaction proceeds with hydrogen abstraction from the $-CH_3$ (methyl) group as the dominant initial step.[8] The atmospheric lifetime of MSAM with respect to its reaction with the OH radical was reported to be about 80 days.[8]

In general, the primary loss process of any atmospheric molecule occurs through its reaction with the OH radical, particularly since the average atmospheric concentration of OH radical is almost 1 order of magnitude higher than that of Cl radical. The experimentally determined rate coefficient cited above for the MSAM + $^\bullet$OH reaction was determined at room temperature[8] and thus the rate coefficients over the entire range of atmospheric temperatures of interest remain unknown. Hence, to begin to assess the relevance and potential consequences of the presence of this newly discovered atmospheric molecule (i.e., MSAM), the present theoretical study sought to accurately calculate the rate coefficients for a range of atmospherically relevant temperatures. In addition, the branching ratios for the MSAM + $^\bullet$OH reaction paths in the studied temperature range were estimated. Accordingly, the rate coefficients for all the site-specific reaction paths and the overall rate coefficients, as well as the branching ratios for the MSAM + $^\bullet$OH reactions, were estimated in the temperature range of 200−400 K. This in turn enabled the estimation of the atmospheric lifetime of MSAM with respect to OH radicals in the studied temperature range. High-level quantum chemistry calculations were used, and based on the results the most plausible degradation mechanism was proposed. Overall, the findings from this study are useful in understanding the oxidation mechanism of various emerging atmospheric pollutants that contain functional groups that have not previously been encountered, such as sulfonamide.

2. COMPUTATIONAL METHODS

2.1. Electronic Structure and Energy Calculations. All the stationary points derived from the MSAM + $^\bullet$OH reaction paths were optimized using the M06-2X hybrid density functional[22] along with Dunning's aug-cc-pV(T + d)Z basis set.[23] This method is believed to provide reliable and effective results in exploring the reaction mechanism of various VOSCs and VOCs under atmospheric conditions.[24−26] The advantage of using the aug-cc-pV(T + d)Z basis set is that it facilitates adding an extra set of tight d-functions which better describe the bonding in sulfur-atom-containing compounds.[27,28] The harmonic vibrational frequencies were computed for all the stable minima and transition states (TSs) at the same M06-2X/aug-cc-pV(T + d)Z level. The keyword OPT = TS implemented in Gaussian 16 was used to locate all of the TSs identified in this work. The calculated frequencies were used to identify the nature of each of the stationary points on the PES as a stable minimum or TS. All TS structures reported in this work possess a single imaginary (negative) frequency, and all other stationary points contain all positive frequencies. The zero-point energy (ZPE) corrections were obtained from the frequency calculations of all the stationary points associated with the MSAM + $^\bullet$OH reaction. The intrinsic reaction coordinate (IRC)[29] calculations were performed at the same level of theory to ensure that all the TSs were connected to the desired pre-reactive and product complexes (PCs). Single point energy calculations were also performed to get more accurate energies for all the minima and TSs using the coupled cluster single and double substitution method with a perturbative treatment of triple excitation (CCSD(T))[30] level with the same aug-cc-pV(T + d)Z basis set. The energy values of all the stationary points were calculated at the CCSD(T)/aug-cc-pV(T + d)Z//M06-2X/aug-cc-pV(T + d)Z (designated as CCSD(T)//M06-2X) level. All ab initio and density functional theory (DFT) calculations presented here were performed using the Gaussian 16 program package.[31] The total electronic energies (E_{total}) and the corresponding ZPE-corrected electronic energies [E_{total}(ZPE)] computed at various levels of theory are displayed in Table S1. The imaginary frequencies of all TSs, rotational constants, vibrational frequencies, and optimized geometries of all the minima and TSs at the M06-2X level are provided in Tables S2−S6 of the Supporting Information.

In addition, the T1 diagnostic in the CCSD single reference calculations was performed to determine the multireference character for all the stationary points associated with the reaction of MSAM + $^\bullet$OH. In general, the larger the T1 value, the less reliable are the results. Based on the literature, T1 values of >0.02 and 0.045 indicate a significant multireference character for closed-shell and open-shell systems, respectively.[32,33] The obtained T1 diagnostic values in the present work are displayed in Table S7 of the Supporting Information. The data from the table indicate that the T1 values for all the stationary points are ≤0.02 for closed-shell systems and <0.045 for open-shell systems, which indicates that the present results are more reliable.

3. RESULTS AND DISCUSSION

3.1. Conformational Analysis. Investigation of the oxidation mechanism of the reaction of MSAM with the OH radical began with the determination of the most stable conformer of MSAM. Accordingly, conformational analysis was performed by rotating the C−S and S−N single bonds associated with MSAM using their corresponding dihedral angles. This process produces several stable conformers, all of which were optimized at the M06-2X/aug-cc-pV(T + d)Z level of theory. The results suggested the two most stable conformers to be the structures shown in Figure 1. These two structures differ from one another by the relative orientation of the two hydrogen atoms of the $-NH_2$ moiety. The structures are labeled *cis*-methane sulfonamide (*cis*-MSAM) and *trans*-methane sulfonamide (*trans*-MSAM) (see Figure 1). In *cis*-MSAM, the two hydrogen atoms on $-NH_2$ are oriented toward the two oxygen atoms of the SO_2 group, whereas in *trans*-MSAM, these hydrogens point in the opposite direction relative to the oxygen atoms of the SO_2 group. Based on the present results computed at the M06-2X/aug-cc-pV(T + d)Z level, the lowest energy conformer is the *cis*-MSAM, which is estimated to be ~1.6 kcal mol^{-1} lower in energy than the *trans*-MSAM (see Figure 1). Thus, the structure of *cis*-MSAM was used as a starting reactant to investigate the reaction with the OH radical in the gas phase.

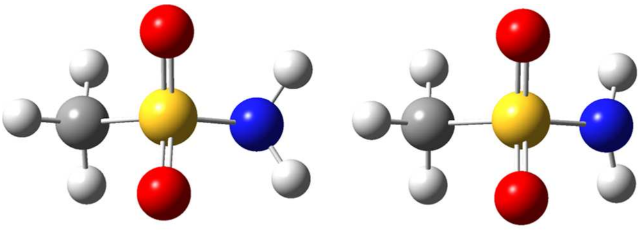
cis-methane sulfonamide
ΔE = 0 kcal mol^{-1}

trans-methane sulfonamide
ΔE = 1.6 kcal mol^{-1}

Figure 1. Conformational structures of MSAM. The relative energies of the two conformers were computed at the M06-2X/aug-cc-pV(T + d)Z level. The energy (kcal mol^{-1}) of the *trans*-MSAM was calculated relative to the energy of the most stable *cis*-MSAM. The black, yellow, white, blue, and red colors represent carbon, sulfur, hydrogen, nitrogen, and oxygen atoms, respectively.

MSAM contains H-atoms bonded to C- and N-atoms of $-CH_3$ and $-NH_2$ groups, respectively. Thus, the atmospheric OH radical is expected to primarily interact with MSAM via abstraction pathways, and the corresponding reactions are shown in eqs 1 and 2. Equation 1 indicates the abstraction of the H-atom from the $-CH_3$ group of MSAM by the OH radical, resulting in the formation of a C-centered MSAM radical ($^{\bullet}CH_2S(=O)_2NH_2$) and molecular water ($H_2O$). Similarly, abstraction by the OH radical of an H-atom from the $-NH_2$ moiety results in the formation of an N-centered MSAM radical ($CH_3S(=O)_2N^{\bullet}H$) and H_2O as products (see eq 2).

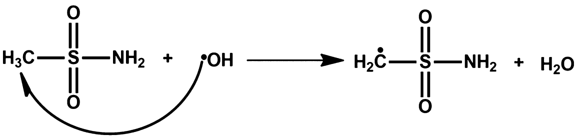
$$H_3C-\overset{O}{\underset{O}{\overset{\|}{\underset{\|}{S}}}}-NH_2 + {}^{\bullet}OH \longrightarrow H_2\dot{C}-\overset{O}{\underset{O}{\overset{\|}{\underset{\|}{S}}}}-NH_2 + H_2O \tag{1}$$

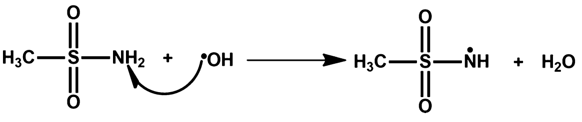
$$H_3C-\overset{O}{\underset{O}{\overset{\|}{\underset{\|}{S}}}}-NH_2 + {}^{\bullet}OH \longrightarrow H_3C-\overset{O}{\underset{O}{\overset{\|}{\underset{\|}{S}}}}-\dot{N}H + H_2O \tag{2}$$

3.2. PES Diagrams for the MSAM + OH Radical Reaction. We first investigated the abstraction paths provided in eqs 1 and 2 by characterizing the corresponding potential energy profiles involving pre-reactive complexes (PRCs), TSs, PCs, and products at the M06-2X/aug-cc-pV(T + d)Z level. The presence of three H-atoms in the $-CH_3$ group should in principle provide three unique OH radical-initiated H-atom abstraction TSs. However, energies calculated at the M06-2X/aug-cc-pV(T + d)Z level indicated only two different TSs. This is mainly due to the equivalency of the two hydrogen atoms that are oriented away from the oxygen atoms of MSAM (see Figure 1). Thus, only two distinct H-atom abstraction TSs are possible for the abstraction of an H-atom from the $-CH_3$ group. These are labeled TS1 and TS2. In addition, the calculations showed the two H-atoms of the $-NH_2$ moiety to be identical, thereby resulting in a single H-atom abstraction TS, which was labeled TS3. Therefore, a total of three different H-atom abstraction TSs are possible for the two abstraction paths associated with the MSAM + $^{\bullet}$OH reaction (see eqs 1 and 2).

The potential energy profiles for the abstraction of an H-atom from the $-CH_3$ group of MSAM with the OH radical (see eq 1) are shown in Figure 2. The energies of all the stationary points on the PES were estimated with respect to the energy of the starting MSAM + OH radical reactants at the CCSD(T)/aug-cc-pV(T + d)Z//M06-2X/aug-cc-pV(T + d)Z (designated as CCSD(T)//M06-2X) level. Based on the PESs shown in Figure 2, abstraction of the H-atom from the $-CH_3$ group of MSAM by the OH radical initially proceeds through the formation of PRCs (PRC1 and PRC2) with binding

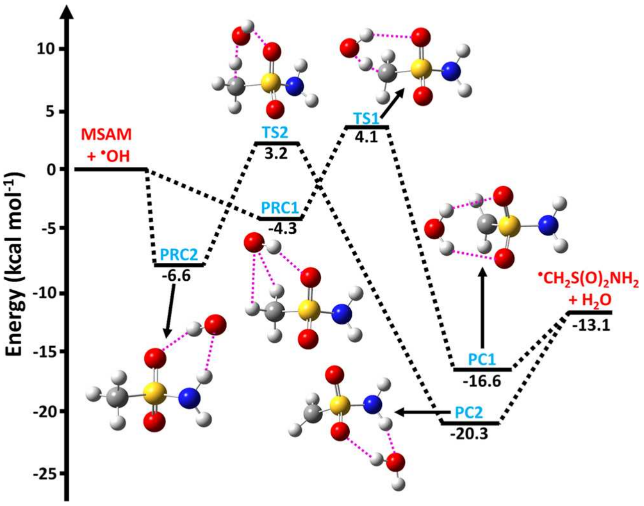

Figure 2. ZPE-corrected PES diagram for the abstraction of H-atom from the $-CH_3$ group of MSAM with the OH radical leading to $^{\bullet}CH_2S(O)_2NH_2 + H_2O$ as products. The energies (kcal mol^{-1}) of all the stationary points were calculated at the CCSD(T)/aug-cc-pV(T + d)Z//M06-2X/aug-cc-pV(T + d)Z level. The symbols PRC1 and PRC2; TS1 and TS2; and PC1 and PC2 refer to "pre-reactive complexes", "transition states", and "product complexes" respectively. The geometries of all the stationary points shown in the figure were optimized at the M06-2X/aug-cc-pV(T + d)Z level. The black, yellow, white, blue, and red colors represent carbon, sulfur, hydrogen, nitrogen, and oxygen atoms, respectively.

energies of −4.3 and −6.6 kcal mol^{-1} below that of the starting reactants. The structures of PRC1 and PRC2 in Figure 2 indicate that the $^{\bullet}OH$ can be attached to MSAM by forming MSAM···OH complexes that are held together by hydrogen bonding. The energies obtained at the CCSD(T)//M06-2X level indicate that PRC2 is ~2.3 kcal mol^{-1} more stable compared to PRC1. The stability of PRC2 is most likely due to strong hydrogen bonding between the OH radical and MSAM. On the other hand, in PRC1, the hydrogen bonding between OH radical and MSAM is weaker in comparison to that in PRC2. The reaction then continues to proceed through the formation of the corresponding TSs (TS1 and TS2) with barrier heights of 4.1 and 3.2 kcal mol^{-1} (respectively) above that of the starting reactants. TS1 and TS2 comprise hydrogen-bonded, six-membered ring-like structures with O···H bond lengths of 2.32 and 2.31 Å, respectively. These TSs lead to the respective PCs (PC1 and PC2) with potential energies of −16.6 and −20.3 kcal mol^{-1}, respectively, relative to the energy of the starting separated reactants. Finally, the PCs undergo unimolecular dissociation to form the same products (i.e., $^{\bullet}CH_2S(=O)_2NH_2 + H_2O$). Based on the PES, it was concluded that the major reaction is the abstraction of an H-atom from the $-CH_3$ group of MSAM by $^{\bullet}OH$, which proceeds through TS2 to form $^{\bullet}CH_2S(=O)_2NH_2 + H_2O$.

We also found a TS for the OH radical-initiated abstraction of the H-atom of the $-CH_3$ group that is oriented away from the O-atoms of the SO_2 group of MSAM and which also leads to the formation of $^{\bullet}CH_2S(=O)_2NH_2 + H_2O$ products. The PES profile associated with this reaction path has an alternative TS, which is shown in Figure S1. Based on the PES, MSAM + $^{\bullet}OH$ initially forms a PRC (PRC2a), which leads to a TS (TS2a) with a barrier height of ~4.7 kcal mol^{-1} relative to the energy of the starting MSAM + OH radical separated reactants. The structure of this alternative TS (TS2a) indicates that the H-atom of the OH radical forms a hydrogen bond with the N-atom of the $-NH_2$ group (see Figure S1). This contrasts with the case of TS2, in which the H-atom of the OH radical forms a hydrogen bond with the O-atom of the SO_2 group (see Figure 2). The formed TS2a then proceeds further to form PC2a and finally to $^{\bullet}CH_2S(=O)_2NH_2 + H_2O$ products. The barrier height of TS2a is ~1.5 kcal mol^{-1} higher than that of the value of TS2. Therefore, we did not consider TS2a for further analysis in our kinetics calculations.

The PES profile for the H-atom abstraction from the $-NH_2$ group of MSAM by the OH radical (eq 2) is shown in Figure 3. It is interesting that the same PRC structure was found for H-atom abstraction from both the $-CH_3$ and $-NH_2$. The reaction then proceeds from PRC2 and then forms a TS (TS3) with a barrier height of 2.3 kcal mol^{-1} above that of the starting reactants (calculated at the CCSD(T)//M06-2X level). The stability of this TS is mainly due to its hydrogen-bonded six-membered ring-like structure, with the hydrogen-bonded O···H bond length being 2.15 Å. The formed TS3 proceeds to produce a PC (PC3), which was located at −17.9 kcal mol^{-1} on the potential, and then finally forms $CH_3S(=O)_2N^{\bullet}H + H_2O$ as separated products. The PES profiles shown in Figures 2 and 3 indicate that abstraction of an H-atom from the $-NH_2$ group of MSAM by the OH radical via PRC2, TS3, and PC3 to form $CH_3S(=O)_2N^{\bullet}H + H_2O$ products has a lower barrier and is energetically more dominant when compared to other possible abstraction paths.

We also verified the barrier heights for all possible H-atom abstraction TSs associated with the MSAM + $^{\bullet}OH$ reaction (eqs 1 and 2) using another level of theory. Specifically, we optimized all possible H-atom abstraction TSs associated with the MSAM + $^{\bullet}OH$ reaction by applying second-order Møller−Plesset (MP2) perturbation theory using the same aug-cc-pV(T + d)Z basis set. All the TSs were verified by performing IRC calculations to determine whether each TS produced correct pre-reactive and PCs. Single-point energy calculations were performed on all the TSs at the CCSD(T)/aug-cc-pV(T + d)Z level by using the previously optimized geometries obtained at the MP2/aug-cc-pV(T + d)Z level. The ZPE-corrected CCSD(T)/aug-cc-pV(T + d)Z//MP2/aug-cc-pV(T + d)Z (designated as CCSD(T)//MP2) level calculated barrier heights for all the TSs are given in Table S8. The data from the table indicate that the barrier heights obtained at the CCSD(T)//M06-2X level agree well with the values obtained at the CCSD(T)//MP2 level. In addition, energy barriers for all the TSs obtained at the CCSD(T)//MP2 and CCSD(T)//M06-2X levels indicate that abstraction of the H-atom from the $-NH_2$ group to form $CH_3S(=O)_2N^{\bullet}H + H_2O$ has a lower barrier and is therefore a more dominant reaction when compared to other possible H-atom abstraction paths.

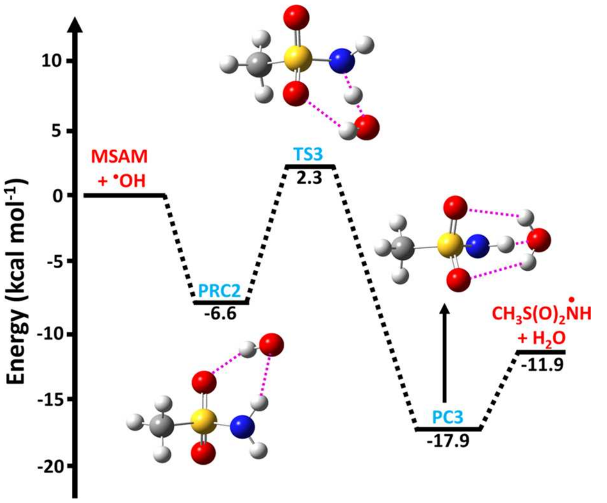

Figure 3. ZPE-corrected PES profile for the abstraction of an H-atom from the $-NH_2$ group of MSAM by OH radical leading to $CH_3S(O)_2N^{\bullet}H + H_2O$ products. The energies (kcal mol^{-1}) of all the stationary points were calculated at the CCSD(T)/aug-cc-pV(T + d)Z//M06-2X/aug-cc-pV(T + d)Z level. The symbols PRC2, TS3, and PC3 refer to "pre-reactive complex", "transition state", and "product complex", respectively. The geometries of all the stationary points shown in the figure were optimized at the M06-2X/aug-cc-pV(T + d)Z level. The black, yellow, white, blue, and red colors represent carbon, sulfur, hydrogen, nitrogen, and oxygen atoms, respectively.

Various theoretical studies have shown that sulfur-atom-containing compounds such as DMS and dimethyl thiosulfinate undergo addition reactions in the presence of OH radical.[34,35] Therefore, calculations were performed for the addition reaction path shown in eq 3, which illustrates the

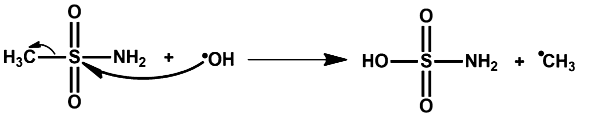

$$H_3C-S(=O)_2-NH_2 + {}^{\bullet}OH \longrightarrow HO-S(=O)_2-NH_2 + {}^{\bullet}CH_3 \quad (3)$$

addition of the O-atom of the OH radical to the S-atom of MSAM, which occurs with simultaneous cleavage of the S−C

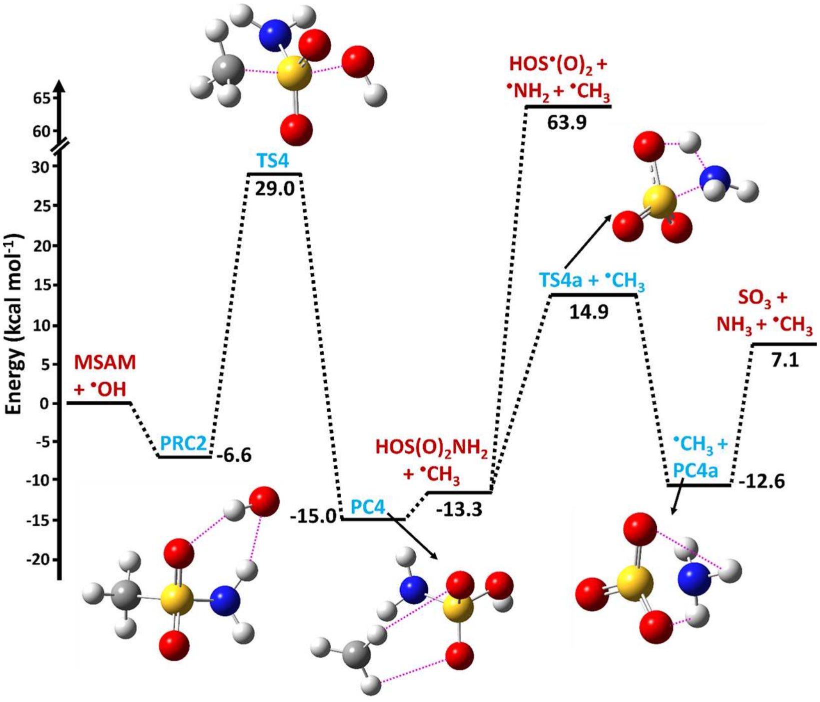

Figure 4. ZPE-corrected potential energy profile for the OH addition pathway involved in the MSAM + OH radical reaction leading to the formation of various products. The energies (kcal mol^{-1}) of all the stationary points were calculated at the CCSD(T)/aug-cc-pV(T + d)Z//M06-2X/aug-cc-pV(T + d)Z level. The symbols PRC2; TS4 and TS4a; and PC4 and PC4a refer to "pre-reactive complex", "transition states", and "product complexes", respectively. The black, yellow, white, blue, and red colors represent carbon, sulfur, hydrogen, nitrogen, and oxygen atoms, respectively.

single bond, leading to the formation of $^{\bullet}CH_3$ + $HOS(O)_2NH_2$ as products.

The PES profile for this OH addition channel (see eq 3) is shown in Figure 4. All of the key stationary points shown in the figure were optimized at the same M06-2X/aug-cc-pV(T + d)Z level. The energies of all the stationary points were calculated at the ZPE-corrected CCSD(T)//M06-2X level. The energies displayed in the figure were estimated relative to the energy of the starting MSAM + $^{\bullet}$OH separated reactants. From Figure 4, the two reactants MSAM and OH radical initially form a PRC (PRC2), which then leads to the corresponding TS (TS4) with a barrier height of ~29.0 kcal mol^{-1}. The structure of TS4 suggests that the O-atom of the OH radical primarily interacts with the S-atom of MSAM to form a new single bond between the S and O-atoms, which is accompanied by simultaneous cleavage of the S−C single bond. The reaction further proceeds from TS4 to form the PC (PC4) at −15.0 kcal mol^{-1}. This then leads to the formation of products $^{\bullet}CH_3$ + $HOS(O)_2NH_2$ at −13.3 kcal mol^{-1} below the starting reactants. The formed $HOS(O)_2NH_2$ undergoes decomposition via two paths. In the first, S−N single-bond fission occurs to form $HOS^{\bullet}(O)_2$ + $^{\bullet}NH_2$ at 63.9 kcal mol^{-1} above the starting MSAM + OH radical reactants. In the second path, $HOS(O)_2NH_2$ proceeds to form a TS (TS4a) by intramolecular H-atom transfer from the OH moiety to the $-NH_2$ group, and this is followed by S−N single-bond fission to form a PC (PC4a), which then leads to SO_3 + NH_3 at 7.1 kcal mol^{-1} above the starting reactants. We included $^{\bullet}CH_3$ in all the steps within the two possible $HOS(O)_2NH_2$ decomposition paths (see Figure 4) in order to factor in its impact on the relative energies of TS4a, PC4a, and the reaction products with the starting MSAM + OH radical reactants. Based on the PES (see Figure 4), the barrier for the $^{\bullet}$OH addition reaction is ~29.0 kcal mol^{-1} above that of the starting reactants. This high barrier is mostly due to the fact that the electron density around the S-atom of MSAM is reduced by the two O-atoms attached to it as well as because of steric hindrance. This is in contrast to the case of DMS, where the high electron density around the S-atom and the reduced steric hindrance enable it to more readily undergo addition to the OH radical. Thus, because of the prohibitively high energy barrier for the OH radical addition, this reaction was not considered for further analysis as it is not accessible under atmospheric conditions.

3.3. PES Diagrams for the *trans*-MSAM + OH Radical Reaction.

Based on the results obtained from the present conformational analysis performed at the M06-2X/aug-cc-pV(T + d)Z level (see Figure 1), *cis*-MSAM is more stable than the *trans*-MSAM by ~1.6 kcal mol^{-1}. Because the energy difference between the *cis*- and *trans*-conformers is relatively small, it is possible that the less stable *trans*-MSAM may also contribute to the overall MSAM + $^{\bullet}$OH reaction. Therefore, we performed calculations on the H-atom abstraction paths associated with the *trans*-MSAM + $^{\bullet}$OH reaction to assess the overall contribution from this conformer. The PES profiles for the abstraction of H-atoms from the $-CH_3$ group of *trans*-MSAM by $^{\bullet}$OH are shown in Figure 5. All the stationary points were optimized at the same M06-2X/aug-cc-pV(T + d)Z level. The energies of all the stationary points were calculated with respect to the starting separated reactants at the ZPE-corrected CCSD(T)//M06-2X level. The resulting PES profiles shown in Figure 5 indicate that the *trans*-MSAM and $^{\bullet}$OH reaction initially proceeds to form barrierless stable PRCs (PRC3 and PRC4) with binding energies of −5.0 and −6.7 kcal mol^{-1}, respectively. These complexes were stabilized by H-bonding interactions. The PRCs then led to the formation

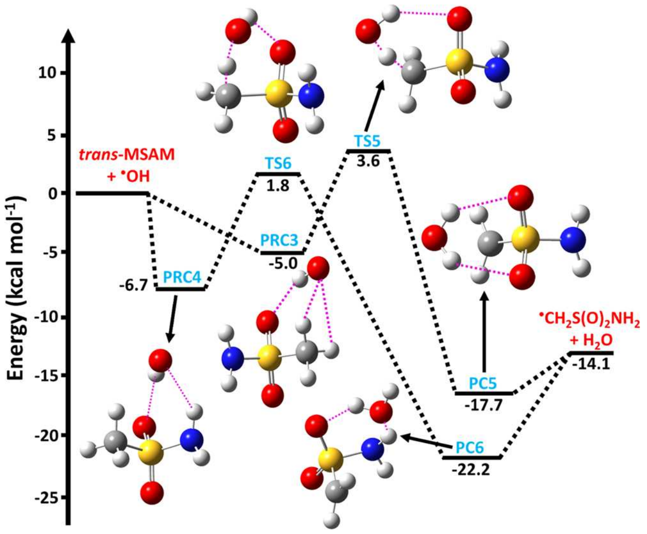

Figure 5. ZPE-corrected PES diagram for the abstraction of an H-atom from the −CH$_3$ group of *trans*-MSAM with the OH radical leading to the formation of $^{\bullet}$CH$_2$S(O)$_2$NH$_2$ + H$_2$O as products. The energies (kcal mol^{-1}) of all the stationary points were calculated at the CCSD(T)/aug-cc-pV(T + d)Z//M06-2X/aug-cc-pV(T + d)Z level. The symbols PRC3 and PRC4; TS5 and TS6; and PC5 and PC6 refer to "pre-reactive complexes", "transition states" and "product complexes" respectively. The black, yellow, white, blue, and red colors represent carbon, sulfur, hydrogen, nitrogen, and oxygen atoms, respectively.

of TSs (TS5 and TS6), with barrier heights of 3.6 and 1.8 kcal mol^{-1}, respectively. The formed TSs then proceed through the corresponding PCs (PC5 and PC6) at −17.7 and −22.2 kcal mol^{-1}, respectively, and then form the same products [i.e., $^{\bullet}$CH$_2$S(O)$_2$NH$_2$ + H$_2$O] at −14.1 kcal mol^{-1}. Based on the results shown in Figure 5, the abstraction of an H-atom from the −CH$_3$ group of *trans*-MSAM by $^{\bullet}$OH through TS6 has a lower barrier and is more dominant compared to other possible paths.

Similarly, the PES diagram for the abstraction of an H-atom from the −NH$_2$ group of *trans*-MSAM by $^{\bullet}$OH is shown in Figure 6. The results reveal that *trans*-MSAM and $^{\bullet}$OH initially form PRC4 and then TS7 with a barrier height of 3.0 kcal mol^{-1} above that of the starting *trans*-MSAM and $^{\bullet}$OH separated reactants. TS7 then proceeds to form CH$_3$S(=O)$_2$N$^{\bullet}$H + H$_2$O products via PC7. A comparison of the abstraction channels involving the *trans*-MSAM + $^{\bullet}$OH reaction that lead to TS6 and TS7 reveals that the abstraction of an H-atom from the −CH$_3$ group via TS6 is energetically more favorable. This result contrasts with that observed for the *cis*-MSAM + $^{\bullet}$OH reaction, where abstraction of an H-atom from the −NH$_2$ group was found to be more dominant. The reason for the difference may be due to the absence of bonding interactions between the H-atoms of the −CH$_3$ group and the lone pair electrons on the N-atom of the −NH$_2$ group (see TS6 structure in Figure 5). This would facilitate easier removal of an H-atom from the C-atom of the −CH$_3$ group in *trans*-MSAM by $^{\bullet}$OH, thereby leading to the lower barrier for this reaction. In contrast, in the case of *cis*-MSAM, the presence of bonding interactions between the H-atoms of the −CH$_3$ group and the lone pair of electrons on the N-atom of the −NH$_2$ group (see TS2 structure in Figure 2) would make H-atom removal more difficult. Therefore, the barrier height for this reaction is higher (see Figures 2 and 5).

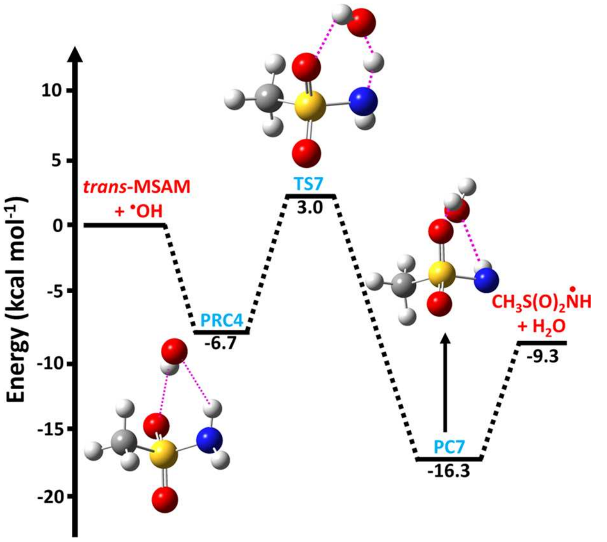

Figure 6. ZPE-corrected PES profile for the abstraction of an H-atom from the −NH$_2$ group of *trans*-MSAM with the OH radical leading to CH$_3$S(O)$_2$N$^{\bullet}$H + H$_2$O as products. The energies (kcal mol^{-1}) of all the stationary points were calculated at the CCSD(T)/aug-cc-pV(T + d)Z//M06-2X/aug-cc-pV(T + d)Z level. The symbols PRC4, TS7, and PC7 refer to "pre-reactive complex", "transition state", and "product complex", respectively. The geometries of all the stationary points shown in the figure were optimized at the M06-2X/aug-cc-pV(T + d)Z level. The black, yellow, white, blue, and red colors represent carbon, sulfur, hydrogen, nitrogen, and oxygen atoms, respectively.

4. KINETIC CALCULATIONS

Rate coefficient calculations are important for understanding the atmospheric fate of MSAM in the presence of OH radicals, as well as the atmospheric implications of the molecules formed from the subsequent oxidation of its reaction products. Therefore, rate coefficients were calculated for three different H-atom abstraction paths associated with the MSAM + $^{\bullet}$OH reaction. The possible abstraction paths shown in the PES profiles occur mainly in two steps (see eq 4). In the first, the MSAM and $^{\bullet}$OH reactants bind via hydrogen bonding to form the corresponding PRC, which is in equilibrium with the separated starting reactants (see eq. 4). In the second step, the formed PRC undergoes unimolecular isomerization via a TS, which then continues to form a PC (see eq 4).

$$\mathrm{MSAM} + {}^{\bullet}\mathrm{OH} \underset{k_{\mathrm{r}}}{\overset{k_{\mathrm{f}}}{\rightleftarrows}} \mathrm{PRC} \xrightarrow{k_{\mathrm{uni}}} \mathrm{PC} \qquad (4)$$

Several experimental and theoretical studies indicate that the presence of a PRC in a bimolecular reaction can influence the reaction dynamics.[36−40] These studies also indicate that the presence of hydrogen-bonded PRCs may result in rate coefficients in the studied temperature range that have a negative temperature dependence. At the same time, several theoretical studies have examined PRCs in the context of reaction mechanisms as well as kinetic modeling. Rate coefficients computed with consideration of PRCs in their kinetic models have been shown to be in excellent agreement with experimentally measured values.[38−40] Therefore, in the present work, we used these same procedures to determine the rate coefficients.

The bimolecular rate coefficients (k) in units of cm^3 molecule^{-1} s^{-1} can be calculated by multiplying the equilibrium constant (K_{eq}) by the unimolecular rate coefficient (k_{uni}), determined over the temperature range of interest using eq 5. It was derived by considering the PRC to be in equilibrium with the starting reactants and to exist under steady state conditions. A similar methodology was followed in several studies for calculating bimolecular rate coefficients.[41−44]

$$k = \left(\frac{k_f}{k_r}\right) k_{uni} = K_{eq} k_{uni} \tag{5}$$

The term K_{eq} in eq 5 represents the formation of a PRC from the starting reactants shown in the first step of eq 4, and it can be represented using $K_{eq} = \frac{k_f}{k_r}$. The symbols k_f and k_r represent the forward and reverse rate coefficients, respectively, for the formation of PRC from MSAM and a radical oxidant (e.g., OH radical). The k_{uni} represents the isomerization of PRC to PC through a TS in the second step, as indicated in eq 4. The equilibrium constant (K_{eq}) was calculated using eq 6, and the unimolecular rate coefficient (k_{uni}) was calculated using canonical variational transition state theory[45−47] (CVT) with the small curvature tunneling[48] (SCT) approach developed in Polyrate (2016) kinetic code[49] as given in eq 7.

$$K_{eq} = \frac{Q_{PRC}}{Q_{MSAM} Q_{OH}} \exp^{-(E_{PRC} - E_{MSAM} - E_{OH})/RT} \tag{6}$$

$$k_{uni}^{CVT/SCT} = \Gamma \frac{k_B T}{h} \frac{Q_{TS}(s^*)}{Q_{PRC}} \exp^{-V(s^*)/RT} \tag{7}$$

In eqs 6 and 7, Q represents the product of the translational, rotational, vibrational, and electronic partition functions of the relevant species. The partition functions were calculated using standard formulas from statistical mechanics.[50] The term E represents the ZPE-corrected energies of the relevant species. R and T represent the ideal gas constant and temperature in Kelvin. Γ is the tunneling factor, which is calculated using the SCT approach. The Boltzmann and Planck constants are represented by k_B and h, respectively, while s^* is the value of the reaction coordinate at the energy maximum. $V(s^*)$ is the potential energy at the barrier maximum.

4.1. Rate Coefficients for the MSAM + •OH Reaction.

We calculated unimolecular step rate coefficients (k_{uni}) at temperatures between 200 and 400 K using the CVT and SCT methods. The obtained values for all three possible abstraction paths are displayed in Table S9. These values were calculated using the ZPE-corrected CCSD(T)//M06-2X energies and vibrational frequencies for all the corresponding species obtained at the M06-2X/aug-cc-pV(T + d)Z level. We also calculated temperature-dependent K_{eq} values in the same studied temperature range for the reaction step involving the formation of PRC from the starting MSAM and •OH reactants, and the values are provided in Table S10. Multiplying k_{uni} by K_{eq} at each studied temperature for the corresponding reaction paths provides the bimolecular rate coefficients. The bimolecular rate coefficients (in cm^3 molecule^{-1} s^{-1}) obtained using this procedure for the three possible abstraction paths associated with the MSAM + •OH reaction in the temperatures between 200 and 400 K are given in Table 1. The data from the table indicate that the bimolecular rate coefficient for the formation of the N-centered MSAM radical ($CH_3S(=O)_2N^{\bullet}H$) + H_2O products through TS3 at 298 K, is ~66 and ~9 times larger than those for the other possible paths that proceed through TS1 and TS2, respectively. For example, the bimolecular rate coefficients for abstraction paths that proceed through TS1 and TS2 at 298 K were 1.6×10^{-15} and 1.2×10^{-14}, respectively, whereas that for TS3 at the same temperature was 1.1×10^{-13} cm^3 molecule^{-1} s^{-1}.

Table 1. Calculated Bimolecular Rate Coefficients for Three Possible H-Atom Abstraction Paths and the Overall Rate Coefficients[a] for the MSAM + OH Radical Reaction at Temperatures between 200 and 400 K

T (K)	k_{TS1}	k_{TS2}[b]	k_{TS3}[b]	$k_{total}^{MSAM+OH}$
200	4.91×10^{-16}	6.42×10^{-15}	1.63×10^{-13}	1.70×10^{-13}
210	5.42×10^{-16}	6.46×10^{-15}	1.43×10^{-13}	1.50×10^{-13}
220	6.07×10^{-16}	6.71×10^{-15}	1.30×10^{-13}	1.37×10^{-13}
230	6.87×10^{-16}	7.04×10^{-15}	1.22×10^{-13}	1.30×10^{-13}
240	7.78×10^{-16}	7.52×10^{-15}	1.16×10^{-13}	1.24×10^{-13}
250	8.87×10^{-16}	8.09×10^{-15}	1.12×10^{-13}	1.21×10^{-13}
260	1.01×10^{-15}	8.71×10^{-15}	1.10×10^{-13}	1.20×10^{-13}
270	1.15×10^{-15}	9.43×10^{-15}	1.09×10^{-13}	1.19×10^{-13}
280	1.31×10^{-15}	1.02×10^{-14}	1.08×10^{-13}	1.19×10^{-13}
290	1.48×10^{-15}	1.11×10^{-14}	1.08×10^{-13}	1.20×10^{-13}
298	1.64×10^{-15}	1.18×10^{-14}	1.09×10^{-13}	1.22×10^{-13}
300	1.68×10^{-15}	1.20×10^{-14}	1.09×10^{-13}	1.22×10^{-13}
400	4.98×10^{-15}	2.63×10^{-14}	1.35×10^{-13}	1.66×10^{-13}

[a] The overall rate coefficients ($k_{total}^{MSAM+OH}$) for the MSAM + OH radical reaction were calculated by adding the rate coefficients for all the individual reaction paths at the corresponding temperatures. [b] The contribution of the rate coefficients through k_{TS2} and k_{TS3} was multiplied by a factor of 2.

The rate coefficients for the reaction through TS3 show slightly negative activation energies (E_a) in the present studied temperature range, even though the barrier for this reaction is +2.3 kcal mol^{-1} relative to that of the starting reactants (see Figure 3 and Table 1). For example, the rate coefficients for this reaction obtained using the CVT/SCT approach were found to be 1.6×10^{-13} and 1.1×10^{-13} cm^3 molecule^{-1} s^{-1} at 200 and 300 K, respectively. The rate coefficients for the same reaction without tunneling were observed to increase with temperature. For example, the rate coefficients without tunneling were computed to be 1.2×10^{-15} and 1.0×10^{-14} cm^3 molecule^{-1} s^{-1} at 200 and 300 K, respectively (see Table 1 and Table S11). This trend is opposite to that observed for the rate coefficient values calculated using the CVT/SCT approach in the same studied temperature range. The change in the behavior in rate coefficients for this reaction calculated using the CVT/SCT approach is clearly due to tunneling (see Table 1).

In addition, the values of the equilibrium constants (K_{eq}) decrease with increasing temperature (see Table S10). This means that as the temperature increases, the equilibrium of the reaction shifts toward the reactant side. As there exists a competition between the unimolecular isomerization of the PRC to the products (via a TS) and reverse decomposition back to the reactants as the temperature increases, the chance of reverse decomposition will be greater than the unimolecular isomerization. However, at the same time, the value of the bimolecular rate coefficients depends on the unimolecular isomerization rate coefficients, as well as on the equilibrium constant, which are determined by the product of both quantities. In this case, the magnitude of the decrease in the equilibrium constant value of PRC2 for the reactants is greater than the increase in the unimolecular isomerization rate coefficient of PRC2 to PC3 via TS3. The equilibrium constants for the formation of the PRC (PRC2) from the starting reactants at 200 and 300 K were found to be 2.8×10^{-18} and 1.1×10^{-20} cm^3 molecule^{-1}, and the corresponding unimolecular rate coefficients (PRC2 → PC3 via TS3) at the same temperatures were found to be 2.9×10^4 and 5.2×10^6 s^{-1}, respectively. Thus, the resultant bimolecular rate coefficients decreased with increasing temperature, which indicates the dominance of the PRC toward this behavior.

In addition, the overall rate coefficient for the atmospheric removal of MSAM in the presence of OH radical was also calculated by adding all the possible abstraction path rate coefficients at each temperature. The obtained overall rate coefficient for the MSAM + $^\bullet$OH reaction in the same studied temperature range is also displayed in Table 1. The overall rate coefficient data in Table 1 indicate that the rate coefficient trend has a slight negative temperature dependence between 200 and 280 K. This is mostly due to the presence of PRCs in the reaction mechanism.

The rate coefficients were also calculated for the more dominant reaction path (TS6) associated with the *trans*-MSAM + $^\bullet$OH reaction to assess its impact on the overall reaction rate. The unimolecular rate coefficient calculated using the CVT/SCT method and the corresponding temperature-dependent equilibrium constant, along with the bimolecular rate coefficients in the temperature range between 200 and 400 K, are given in Table S12. We also calculated the weight factors for the *trans*-MSAM from the Boltzmann distribution function. The weight factors of *cis*-MSAM and *trans*-MSAM can be calculated using equations $\Gamma1 = 1/(1 + \exp(-\Delta G/RT))$ and $\Gamma2 = 1 - \Gamma1$, respectively, where $\Gamma1$ and $\Gamma2$ are the weight factors of *cis*-MSAM and *trans*-MSAM, respectively, and ΔG is the Gibbs free energy difference between the two conformers. The obtained weight factors for the *trans*-MSAM in the temperature range between 200 and 400 K are given in Table S12. The results indicate that the weight factors ($\Gamma2$) for *trans*-MSAM are 0.014 at 200 K and 0.055 at 300 K. The rate coefficients calculated using the weight factors for the major reaction via TS6 for the *trans*-MSAM + $^\bullet$OH reaction at 200 and 300 K are 2.0×10^{-15} and 5.4×10^{-15} cm^3 molecule^{-1} s^{-1}, respectively. This indicates that the rate coefficient for the *trans*-MSAM + $^\bullet$OH reaction is ~2 orders of magnitude smaller than that of the *cis*-MSAM + $^\bullet$OH reaction. Therefore, the contribution from the *trans*-conformer is not significant, and hence we did not proceed further in calculating the rate coefficients for other remaining H-abstraction paths, which have higher barriers and represent minor paths associated with the *trans*-MSAM + $^\bullet$OH reaction.

The energy barriers for the unimolecular reaction steps (PRCs → TSs) are all positive and higher than 8.4 kcal mol^{-1} for the present studied H-abstraction reactions (see Figures 2, 3, and 5), suggesting that tunneling may contribute significantly to the MSAM + $^\bullet$OH reaction system. The calculated SCT contributions are given in Table S11 for all possible H-atom abstraction paths at temperatures between 200 and 400 K. The results indicate that SCT contributions are significant from 200 to 250 K, beyond which they gradually decrease for all possible abstraction paths. For example, the SCT contribution for the major products $CH_3S(=O)_2N^\bullet H$ + H_2O via TS3 was found to be $\sim 1.40 \times 10^2$ at 200 K, which decreased to 4.13 at 400 K.

Branching ratio calculations were performed to ascertain the percentage contributions to the overall MSAM + $^\bullet$OH reaction from each specific H-atom abstraction site. The contribution of each H-abstraction site to the overall reaction was estimated from the ratio of individual H-abstraction site rate coefficients and the overall rate coefficient at the respective temperature. The calculated branching ratio values in percentages for all possible MSAM + $^\bullet$OH reactions are displayed in Table S13. The data from the table indicate that the contribution from the major reaction (TS3) decreases with increasing temperature from ~95.9% at 200 K to 81.2% at 400 K. For the second major reaction (TS2), the contribution increases from 3.8% at 200 K to 15.8% at 400 K. The other reaction path contributions via TS1 are negligible from 200 to 240 K, but then gradually increase with temperature to a contribution of 3.0% at 400 K. The branching ratio calculations suggest that $CH_3S(=O)_2N^\bullet H$ and H_2O are the major products of the MSAM + $^\bullet$OH reaction.

4.2. Atmospheric Implications. The overall rate coefficients for the MSAM + $^\bullet$OH reaction at 298 K were found to be 1.2×10^{-13} cm^3 molecule^{-1} s^{-1}, which is ~18, $\sim 7.4 \times 10^2$, and $\sim 4.8 \times 10^2$ times smaller than the values for the DMS (CH_3SCH_3) + $^\bullet$OH (2.2×10^{-12} cm^3 molecule^{-1} s^{-1}),[51] methanesulfinic acid ($CH_3S(=O)OH$) + $^\bullet$OH (9.0×10^{-11} cm^3 molecule^{-1} s^{-1}),[52] and dimethyl sulfoxide ($CH_3S(=O)CH_3$) + $^\bullet$OH (5.9×10^{-11} cm^3 molecule^{-1} s^{-1})[9] reactions, respectively. In addition, the MSAM + $^\bullet$OH reaction rate coefficient at 298 K is close to the value for the dimethyl sulfone ($CH_3S(=O)_2CH_3$) + $^\bullet$OH reaction, which has a reported rate coefficient of $<3.0 \times 10^{-13}$ cm^3 molecule^{-1} s^{-1}.[9] This suggests that the lifetime of MSAM with respect to $^\bullet$OH at 298 K is higher than those for DMS, methanesulfinic acid, dimethyl sulfoxide, and dimethyl sulfone at the same temperature.[8]

The removal of gas-phase molecules in the troposphere is controlled by various processes such as photolysis and reactions with OH radical, nitrate (NO_3) radical, and/or ozone (O_3). In the case of MSAM, the absence of a C=C in its structure would make its reaction with O_3 slow. This supposition is supported by the observation that the reaction of MSAM with O_3 proceeds only to a negligible extent over a period of several hours. Based on this finding, the upper limit rate coefficient for this reaction was reported to be 1.0×10^{-19} cm^3 molecule^{-1} s^{-1},[8] and it suggests that the removal of MSAM via its reaction with O_3 is negligible under tropospheric conditions.[8] This study also reported that the MSAM reaction with NO_3 radical is not an important removal process in the troposphere, mainly because of the decrease in electron density around the S-atom of MSAM due to its bonding to two O-atoms. Also, the NO_3 radical cannot readily form a PRC with the S-atom of MSAM due to steric hindrance. It was further reported that photolysis of MSAM as a mechanism of removal is negligible under tropospheric conditions.[8] Therefore, the atmospheric fate of MSAM mostly depends on its reaction with $^\bullet$OH. The lifetime of MSAM can be calculated using the general formula $\tau = 1/(k_{\text{overall}}[\text{OH}])$,[53] where k_{overall} is the overall rate coefficient for the MSAM + $^\bullet$OH reaction and [OH] is the average tropospheric concentration of the OH radical ([OH] = 1.0×10^6 molecule cm^{-3}). The rate coefficient data obtained from the present work were used to calculate the atmospheric lifetime of MSAM with the OH radical. The estimated lifetime of MSAM with respect to $^\bullet$OH was found to be ∼68−97 days at the temperatures between 200 and 400 K.

4.3. $CH_3S(=O)_2N^{\bullet}H + {}^3O_2$ Reaction.

The energetics and kinetics results obtained for the MSAM + $^{\bullet}OH$ reaction indicate that the dominant path results in the formation of $CH_3S(=O)_2N^{\bullet}H + H_2O$ under atmospheric conditions. This study is the first to identify the reaction of MSAM with $^{\bullet}OH$ as exclusively generating N-centered MSAM radicals. Once released, $CH_3S(=O)_2N^{\bullet}H$ is expected to undergo unimolecular dissociation via C−S bond fission or react with atmospheric oxygen ($^3O_2$). Based on the findings of Berasategui et al.,[8] the formed $CH_3S(=O)_2N^{\bullet}H$ radical does not undergo unimolecular dissociation via C−S bond fission to form CH_3 radical and $S(=O)_2NH$ radical, since the characteristic IR-absorption bands indicative of the presence of the $S(=O)_2NH$ product were not observed. In addition, they reported that the C−S bond fission reaction is endothermic by 137 kJ mol^{-1} at the G4MP2 level. This suggests that unimolecular dissociation of $CH_3S(=O)_2N^{\bullet}H$ through a C−S single bond reaction is not feasible. On the other hand, $CH_3S(=O)_2N^{\bullet}H$ can react with the relatively large concentrations of O_2 molecules present under tropospheric conditions.[54] The concentration of MSAM detected in the ocean atmosphere was in the range of 20−50 ppt, indicating that the fate of $CH_3S(=O)_2N^{\bullet}H$ is important in order to fully understand the transformation mechanism of MSAM and its final reaction products. The PES profile associated with the $CH_3S(=O)_2N^{\bullet}H + {}^3O_2$ reaction is shown in Figure 7. The stationary point geometries of reactants, intermediates, TSs, and products were optimized at the same M06-2X/aug-cc-pV(T + d)Z level cited previously. The energies of all the stationary points displayed on the PES profiles shown in Figure 7 were calculated at the ZPE-corrected CCSD(T)//M06-2X level using the same basis set. The stationary point energies were calculated relative to the energy of the $CH_3S(=O)_2N^{\bullet}H + {}^3O_2$ starting reactants. The resulting PES profile suggests that the addition of O_2 to the N-centered MSAM-radical proceeds via formation of TS8 with a barrier height of ∼7.6 kcal mol^{-1}. We note that a similar TS has been observed in the addition of $CH_3N^{\bullet}H$ to ground-state oxygen to form the CH_3NHOO radical adduct.[55] The barrier height for this reaction was reported to be 2.5 kcal mol^{-1} at the G3X-K level of theory.[55] In the present work, the barrier height for the formation of the RO_2 radical adduct through TS8 is ∼5 kcal mol^{-1} higher than the value for the RO_2 radical adduct formed from the $CH_3N^{\bullet}H + O_2$ reaction.[55] The significant difference in barrier heights may be due to differences between the molecular structures of $CH_3S(=O)_2N^{\bullet}H$ and $CH_3N^{\bullet}H$, but it could also be a consequence of the fact that two different computational methods were used in estimating the energies. TS8 then proceeds to form the RO_2 radical adduct (where R = $CH_3S(=O)_2NH$). In principle, two reaction types[56−59] are possible for the degradation of the RO_2 radical adduct: (1) unimolecular reactions and (2) bimolecular reactions with the hydroperoxyl (HO_2) radical or nitric oxide (NO). The competition between unimolecular and bimolecular reactions associated with any RO_2 radical primarily depends on the kinetic parameters of the unimolecular and bimolecular reactions, as well as the average atmospheric concentration of HO_2 radicals and NO in ambient air.[58,59] Therefore, to get a better understanding of the unimolecular reaction mechanism and the fate of the $CH_3S(=O)_2NHOO$ radical adduct, the PES profiles involving the stationary point geometries and energies were computed. The results are shown in Figure 7. We considered intramolecular hydrogen shift (H-shift) reactions as an important unimolecular reaction channel, since various studies have shown that unimolecular reactions are important pathways for the transformation of RO_2 radicals.[60−62] Because the $CH_3S(=O)_2NHOO$ radical has H-atoms bonded to both C- and N-atoms, two H-shift reactions are possible: (i) transfer of an H-atom from the N to the terminal O-atom of the RO_2 radical via TS9 with a barrier height of 31.3 kcal mol^{-1} above that of the $CH_3S(=O)_2N^{\bullet}H + O_2$ reactants. The formed TS9 then proceeds to form the corresponding QOOH (Q = $CH_3S(=O)_2N^{\bullet}$) radical (PC8); and (ii) H-atom transfer from the C-atom of the $-CH_3$ group to the terminal O-atom of the RO_2 group through TS10, with a barrier height of 33.1 kcal mol^{-1} above that of the $CH_3S(=O)_2N^{\bullet}H + O_2$ reactants. The formed TS then proceeds to the corresponding QOOH (Q = $^{\bullet}CH_2S(=O)_2NH$) radical (PC9). The barrier heights for the two possible H-shift reactions are above 30 kcal mol^{-1}, which indicates that these paths were not accessible under atmospheric conditions, although they may be feasible under high-temperature conditions.

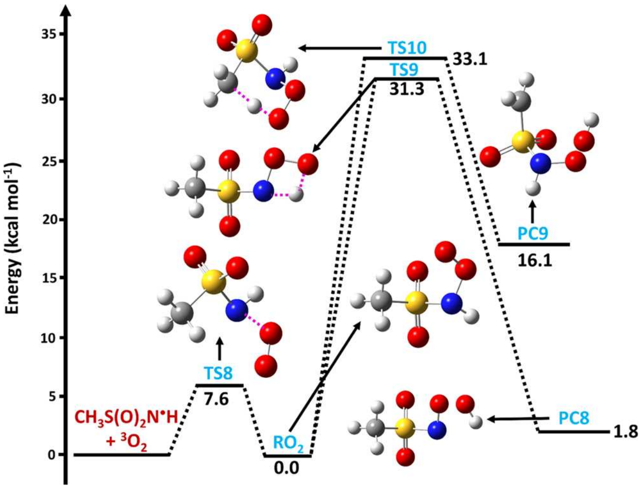

Figure 7. ZPE-corrected potential energy surface profile for the $CH_3S(=O)_2N^{\bullet}H + {}^3O_2$ reaction. The energies (kcal mol^{-1}) of all the stationary points on the potential were obtained at the CCSD(T)/aug-cc-pV(T + d)Z//M06-2X/aug-cc-pV(T + d)Z level. The symbols TS8, TS9, and TS10 refer to the indicated transition states; RO_2: $CH_3S(=O)_2NHOO^{\bullet}$; PC8: $CH_3S(=O)_2N^{\bullet}OOH$; and PC9: $^{\bullet}CH_2S(=O)_2NOOH$. The geometries of all the stationary points shown in the figure were optimized at the M06-2X/aug-cc-pV(T + d)Z level. The black, yellow, white, blue, and red colors represent carbon, sulfur, hydrogen, nitrogen, and oxygen atoms, respectively.

4.4. Reaction of the RO_2 Radical ($CH_3S(=O)_2NHOO^{\bullet}$) with HO_2 Radical/NO.

The energy barriers for the unimolecular dissociation of $CH_3S(=O)_2NHOO^{\bullet}$ are very high, indicating that this reaction would proceed very slowly under atmospheric conditions. Therefore, the fate of $CH_3S(=O)_2NHOO^{\bullet}$ mainly depends on its reactions with HO_2 radicals/NO. The reaction of $CH_3S(=O)_2NHOO^{\bullet}$ with the HO_2 radical primarily proceeds to form the corresponding hydroperoxide ($CH_3S(=O)_2NHOOH$) + O_2 products as shown in eq 8.

The typical reaction rate coefficient for the $RO_2 + HO_2$ radical reaction[58] has been reported to be 8.14×10^{-12} cm^3 molecule^{-1} s^{-1} at 298 K, and the concentration of HO_2 radicals

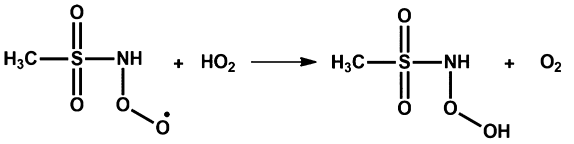

$$H_3C-S(=O)_2-NH-O-O^\bullet + HO_2 \longrightarrow H_3C-S(=O)_2-NH-O-OH + O_2 \quad (8)$$

in the remote pristine atmosphere, urban atmosphere in the afternoon, and even in indoor air is ~40 ppt.[63] Thus, in calculating the pseudo-first-order rate coefficient, the typical RO_2 + HO_2 reaction rate coefficient and the average concentration of HO_2 radicals in the remote pristine atmosphere were used. Based on these values, the calculated pseudo-first-order rate coefficient for the $CH_3S(=O)_2NHOO^\bullet$ + HO_2 radical reaction was found to be ~8.14 × 10^{-3} s^{-1} at 298 K. This suggests that the bimolecular reaction of RO_2 + HO_2 radicals is significantly faster than the RO_2 unimolecular reactions. Similarly, $CH_3S(=O)_2NHOO^\bullet$ can react with NO to form the corresponding radical ($CH_3S(=O)_2NHO^\bullet$) + nitrogen dioxide (NO_2) as shown in eq 9.

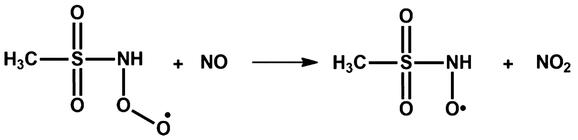

$$H_3C-S(=O)_2-NH-O-O^\bullet + NO \longrightarrow H_3C-S(=O)_2-NH-O^\bullet + NO_2 \quad (9)$$

This reaction is another possible competitive path for the unimolecular dissociation of the RO_2 radical. The pseudo-first-order rate coefficient for the RO_2 + NO reaction was found to be 2.30 × 10^{-2} s^{-1} at 298 K. In calculating this rate coefficient, we used the RO_2 + NO reaction rate coefficient of 9.0 × 10^{-12} cm^3 $molecule^{-1}$ s^{-1}, and an NO concentration of ~100 ppt that has been reported in the remote pristine atmosphere and in urban atmospheres.[59,64,65] Therefore, the $CH_3S(=O)_2NHOO^\bullet$ + HO_2, and $CH_3S(=O)_2NHOO^\bullet$ + NO reactions are more dominant than the unimolecular reactions of $CH_3S(=O)_2NHOO^\bullet$.

4.5. MSAM + OH Radical Mechanism. For the MSAM + OH radical reaction, we propose a mechanism that is based on the results observed in the present work and experimental findings reported in the recent literature.[8] The details for this OH radical-initiated oxidation of MSAM are shown in Figure 8. In the first primary step, the OH radical abstracts an H-atom from the $-NH_2$ group of MSAM, yielding $CH_3S(=O)_2N^\bullet H$ + water. $CH_3S(=O)_2N^\bullet H$ then reacts with $^3O_2$ to form the RO_2 radical adduct ($CH_3S(=O)_2NHOO^\bullet$). As our results indicate that unimolecular dissociation reactions for the RO_2 radical are very slow compared to RO_2 + HO_2 and RO_2 + NO reactions, it is proposed that the RO_2 radical adduct proceeds down one of two paths: (1) (illustrated with red arrows in Figure 8) $CH_3S(=O)_2NHOO^\bullet$ can be intercepted by the HO_2 radical to form $CH_3S(=O)_2NHOOH$ + O_2 products. The formed $CH_3S(=O)_2NHOOH$ then undergoes a reaction with the OH radical. Various H-abstraction channels are possible for the $CH_3S(=O)_2NHOOH$ + $^\bullet OH$ reaction (see eqs 10–12).

$$CH_3S(=O)_2NHOOH + {}^\bullet OH \xrightarrow{\Delta E_0^\ddagger = 2.6\ \mathrm{kcal\ mol^{-1}}} {}^\bullet CH_2S(=O)_2NHOOH + H_2O \quad (10)$$

$$CH_3S(=O)_2NHOOH + {}^\bullet OH \xrightarrow{\Delta E_0^\ddagger = -2.6\ \mathrm{kcal\ mol^{-1}}} CH_3S(=O)_2N^\bullet OOH + H_2O \quad (11)$$

$$CH_3S(=O)_2NHOOH + {}^\bullet OH \xrightarrow{\Delta E_0^\ddagger = -1.9\ \mathrm{kcal\ mol^{-1}}} CH_3S(=O)_2NHOO^\bullet + H_2O \quad (12)$$

To know the most preferred abstraction path from the reactions given in eqs 10–12, calculations were performed on optimizing the possible TSs at the M06-2X/cc-pVTZ level. The barrier heights for all the TSs for the reactions given in eqs 10–12 were calculated at the same M06-2X/cc-pVTZ level of theory. The optimized TS structures and the corresponding barrier heights are shown in Figure S2 for the reactions in eqs 10–12. The results indicate that the abstraction of the H-atom attached to the N-atom of $CH_3S(=O)_2NHOOH$ by the OH radical through TS14, leading to $CH_3S(=O)_2N^\bullet OOH$ + H_2O as products (eq 11) had the lowest barrier (−2.6 kcal mol^{-1}) and was more dominant compared to the other possible paths. $CH_3S(=O)_2N^\bullet OOH$ further undergoes O–O single bond scission to form $CH_3S(=O)_2NO$ + $^\bullet OH$ as products (see Figure 8). The fate of $CH_3S(=O)_2NO$ is a reaction with the OH radical to form $^\bullet CH_2S(=O)_2NO$, which may further react with O_2 to form $^\bullet OOCH_2S(=O)_2NO$. This then reacts with the HO_2 radical to form the corresponding peroxide ($HOOCH_2S(=O)_2NO$). The likely fate of $HOOCH_2S(=O)_2NO$ is a reaction with the OH radical. Two different H-atom abstraction paths (see eqs 13 and 14) were expected for the $HOOCH_2S(=O)_2NO$ + $^\bullet OH$ reaction.

$$HOOCH_2S(=O)_2NO + {}^\bullet OH \rightarrow {}^\bullet OOCH_2S(=O)_2NO + H_2O \quad (13)$$

$$HOOCH_2S(=O)_2NO + {}^\bullet OH \rightarrow HOO^\bullet CHS(=O)_2NO + H_2O \quad (14)$$

The rate coefficients for the H-atom abstraction from the peroxide group (eq 13) and the adjacent carbon (eq 14) are close to 1–5 × 10^{-12} cm^3 $molecule^{-1}$ s^{-1}.[8] This rate coefficient was taken from the CH_3OOH + $^\bullet OH$ reaction for comparison. This suggests that the rates for the reactions given in eqs 13 and 14 are almost the same. In addition, the reaction given in eq 13 reproduces the peroxy radical ($^\bullet OOCH_2S(=O)_2NO$), whereas the $HOO^\bullet CHS(=O)_2NO$ formed from the reaction given in eq 14 undergoes C–S single bond cleavage to form formic acid and $^\bullet S(=O)_2NO$. The formed $^\bullet S(=O)_2NO$ further undergoes S–N single bond scission to form SO_2 and $^\bullet NO$ as final products. (2) (shown with blue arrows in Figure 8) RO_2 radical (i.e., $CH_3S(=O)_2NHOO^\bullet$) is intercepted by NO, leading to the formation of $CH_3S(=O)_2NHO^\bullet$ and release of NO_2. The $CH_3S(=O)_2NHO^\bullet$ then undergoes S–N single-bond cleavage to give HNO and $CH_3S^\bullet(=O)_2$ as products. The fate of $CH_3S^\bullet(=O)_2$ in the atmosphere has been previously reported to involve extrusion of SO_2 with concomitant release of the CH_3 radical via C–S bond scission.[25] The CH_3 radical then reacts with $^3O_2$ to form the OH radical and formaldehyde (HC(O)H) via the $CH_3OO^\bullet$ adduct. The fate of formaldehyde in the presence of OH and O_2 involves a series of reactions ultimately resulting in the

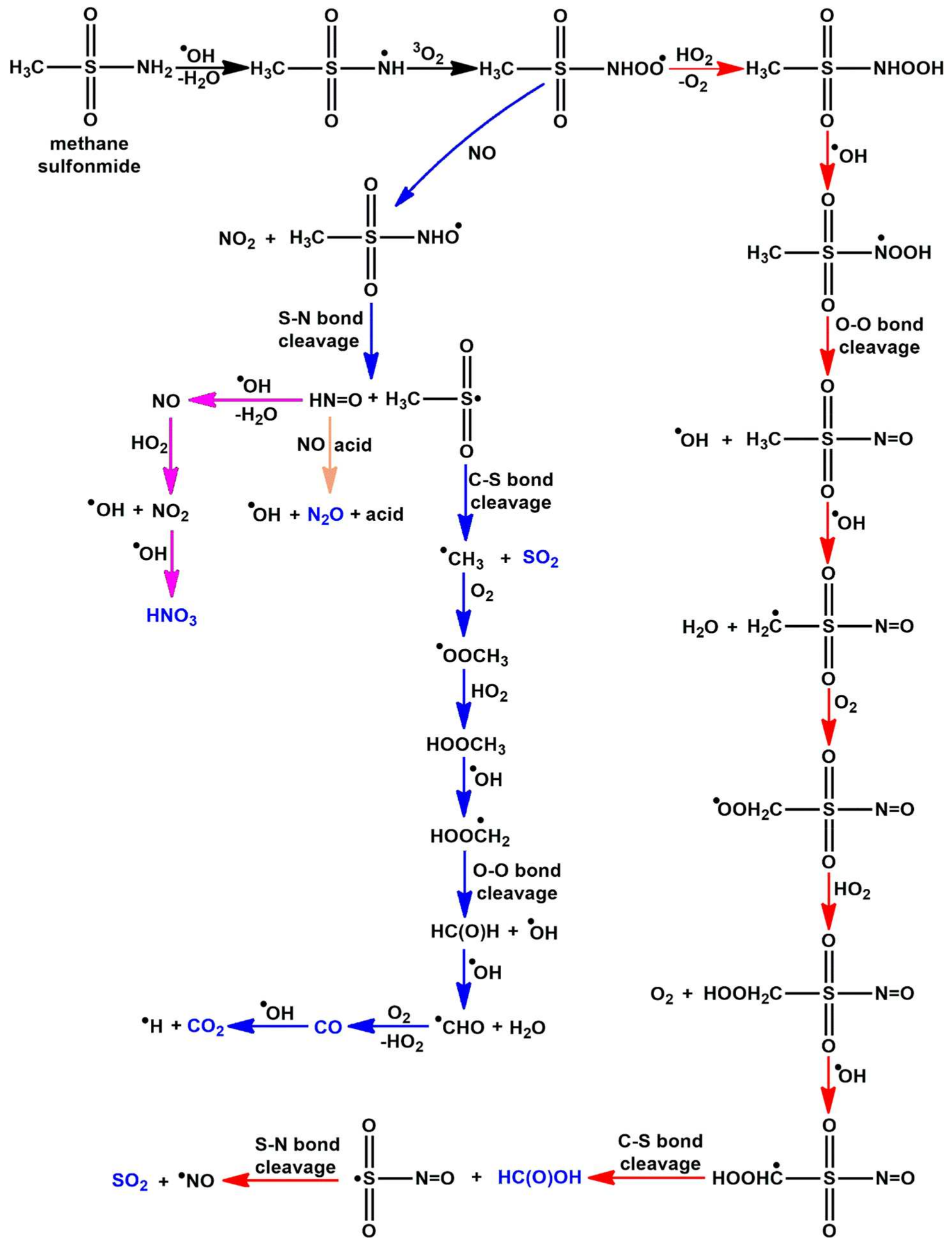

Figure 8. Proposed mechanism for the degradation of MSAM initiated by the OH radical in the presence of ground state $^3O_2$, HO_2 radical, and NO under tropospheric conditions. SO_2, HC(=O)OH, HNO_3, N_2O, CO, and CO_2 have been experimentally observed in the reaction of MSAM with the OH radical at 298 K.[8]

formation of CO and CO_2 as final products.[8] The fate of HNO in the presence of OH and HO_2 radicals is indicated using pink-colored arrows in Figure 8, and results in the formation of HNO_3 as the final product. The alternative fate of HNO is reaction with NO, leading to the formation of N_2O + •OH as final products (indicated with an orange arrow). The rate coefficient for the HNO + NO → N_2O + •OH reaction was reported to be >9.9 × 10^{-17} cm^3 $molecule^{-1}$ s^{-1} at 300 K.[66] This suggests that it is slow and cannot be the source of N_2O at room temperature. Another possibility for the formation of N_2O is expected from the decomposition of the initially formed $CH_3S(O)_2NH$ radical through S−N bond fission, leading to the formation of $CH_3S^{\bullet}(O)_2$ + NH (i.e., nitrene) (see eq 15). The formed NH would react with NO to form N_2O and •H as products (see eq 16). However, we calculated the free energy of the reaction shown in eq 15 at the M06-2X/6-311++G(2d,2p) level of theory, and the results indicate that it is non-spontaneous by 48 kcal mol^{-1}. Therefore, we conclude that the reactions shown in eqs 15 and 16 are also not the source for N_2O.

$$CH_3S(O)_2NH \rightarrow CH_3S^{\bullet}(O)_2 + NH \tag{15}$$

$$NH + NO \rightarrow N_2O + {}^{\bullet}H \tag{16}$$

However, several studies indicate that formic acid and nitric acid can reduce the energy barriers for many atmospheric reactions.[42,67] Given that the MSAM + •OH reaction produces formic and nitric acids as products, these compounds may serve as catalysts for the HNO + NO reaction, promoting their occurrence at room temperature by reducing the reaction barrier significantly, resulting in the formation of N_2O + OH radical products (see Figure 8). Thus, these reaction cascades and their resulting products reveal that the oxidation of MSAM initiated by the OH radical results in the formation of pollutants such as SO_2, HC(=O)OH, HNO_3, N_2O, CO, and CO_2. Importantly, the SO_2, HC(=O)OH, HNO_3, N_2O, CO, and CO_2 products predicted by the theoretical calculations conducted in this work for the reaction of MSAM with OH radical fully align with those that were experimentally observed at 298 K.[8] The overall results suggest that the emission of MSAM from the oceans has the potential to impact global warming, acid rain production, and the formation of secondary organic aerosols (SOA).

5. CONCLUSIONS

The energetics for the atmospheric oxidation reaction of MSAM initiated by the OH radical, followed by subsequent transformation of the immediate $CH_3S(=O)_2N^{\bullet}H$ product in the presence of $^3O_2$, were investigated using ab initio/DFT electronic structure calculations. The rate coefficients for all possible H-atom abstraction paths were calculated using the CVT/SCT approach. The main findings from the results are summarized below:

(i) The energetics, rate coefficients, and branching ratio data indicate that abstraction of the H-atom from the NH_2 group of MSAM by the OH radical to form $CH_3S(=O)_2N^{\bullet}H + H_2O$ as products is the dominant reaction when compared to other possible abstraction paths.
(ii) The barrier for the OH radical addition to the S-atom of MSAM to form products $^{\bullet}CH_3 + HOS(O)_2NH_2$ is ∼29.0 kcal mol^{-1} above that of the starting reactants. This indicates that this reaction path is not accessible under atmospheric conditions.
(iii) The rate coefficient for the overall decomposition of MSAM through its interaction with the OH radical is estimated to be 1.2×10^{-13} cm^3 $molecule^{-1}$ s^{-1} at 298 K, which is in excellent agreement with the reported experimentally measured value (1.4×10^{-13} cm^3 $molecule^{-1}$ s^{-1}) determined at the same temperature.
(iv) The lifetime of MSAM with respect to its reaction with the OH radical is estimated to be ∼68−97 days at temperatures between 200 and 400 K.
(v) The most plausible degradation mechanism of MSAM involves abstraction by $^{\bullet}OH$ of an H-atom from the amino group of MSAM, followed by reaction of the product with atmospheric O_2 and HO_2 radical/NO, leading to the formation of SO_2, CO, CO_2, N_2O, HC(=O)OH, and HNO_3 as final products.
(vi) The present results suggest that MSAM emissions from the oceans may have significant effects on global warming, acid rain, and formation of SOAs.

■ ASSOCIATED CONTENT

Supporting Information

The Supporting Information is available free of charge at https://pubs.acs.org/doi/10.1021/acs.jpca.2c06432.

Calculated total electronic energies including zero-point energy corrections, imaginary frequencies of various TSs, rotational constants, optimized geometries of all the stationary points, vibrational frequencies, unimolecular rate coefficients, equilibrium constants, tunneling contributions, branching ratios, PES diagram, optimized geometries, and barrier heights for various TSs (PDF)

■ AUTHOR INFORMATION

Corresponding Author

Rabi A. Musah − *Department of Chemistry, University at Albany—State University of New York, Albany, New York 12222, United States;* orcid.org/0000-0002-3135-4130; Email: rmusah@albany.edu

Author

Parandaman Arathala − *Department of Chemistry, University at Albany—State University of New York, Albany, New York 12222, United States*

Complete contact information is available at: https://pubs.acs.org/10.1021/acs.jpca.2c06432

Notes

The authors declare no competing financial interest.

■ ACKNOWLEDGMENTS

Financial support of the National Science Foundation (grant numbers 1310350 and 1710221) to R.A.M. is gratefully acknowledged. The authors are also grateful for the support of the High-Performance Computing Center at the University at Albany-SUNY.

■ REFERENCES

(1) Bentley, R.; Chasteen, T. G. Environmental VOSCs−−formation and degradation of dimethyl sulfide, methanethiol and related materials. *Chemosphere* **2004**, *55*, 291−317.

(2) Andreae, M. O. Ocean-atmosphere interactions in the global biogeochemical sulfur cycle. *Mar. Chem.* **1990**, *30*, 1−29.

(3) Bates, T. S.; Lamb, B. K.; Guenther, A.; Dignon, J.; Stoiber, R. E. Sulfur emissions to the atmosphere from natural sourees. *J. Atmos. Chem.* **1992**, *14*, 315−337.

(4) Spiro, P. A.; Jacob, D. J.; Logan, J. A. Global inventory of sulfur emissions with 1° × 1° resolution. *J. Geophys. Res.* **1992**, *97*, 6023−6036.

(5) Charlson, R. J.; Lovelock, J. E.; Andreae, M. O.; Warren, S. G. Oceanic phytoplankton, atmospheric sulphur, cloud albedo and climate. *Nature* **1987**, *326*, 655−661.

(6) Andreae, M. O.; Crutzen, P. J. Atmospheric aerosols: Biogeochemical sources and role in atmospheric chemistry. *Science* **1997**, *276*, 1052−1058.

(7) Edtbauer, A.; Stönner, C.; Pfannerstill, E. Y.; Berasategui, M.; Walter, D.; Crowley, J. N.; Lelieveld, J.; Williams, J. A new marine biogenic emission: Methane sulfonamide (MSAM), dimethyl sulfide (DMS), and dimethyl sulfone ($DMSO_2$) measured in air over the Arabian Sea. *Atmos. Chem. Phys.* **2020**, *20*, 6081−6094.

(8) Berasategui, M.; Amedro, D.; Edtbauer, A.; Williams, J.; Lelieveld, J.; Crowley, J. N. Kinetic and mechanistic study of the reaction between methane sulfonamide ($CH_3S(O)_2NH_2$) and OH. *Atmos. Chem. Phys.* **2020**, *20*, 2695−2707.

(9) Falbe-Hansen, H.; Sørensen, S.; Jensen, N. R.; Pedersen, T.; Hjorth, J. Atmospheric gas-phase reactions of dimethylsulphoxide and dimethylsulphone with OH and NO_3 radicals, Cl atoms and ozone. *Atmos. Environ.* **2000**, *34*, 1543−1551.

(10) Voss, M.; Bange, H. W.; Dippner, J. W.; Middelburg, J. J.; Montoya, J. P.; Ward, B. The marine nitrogen cycle: Recent discoveries, uncertainties and the potential relevance of climate change. *Philos. Trans. R. Soc., B* **2013**, *368*, 20130121.

(11) Ge, X.; Wexler, A. S.; Clegg, S. L. Atmospheric amines − Part I. A review. *Atmos. Environ.* **2011**, *45*, 524−546.

(12) Gibb, S. W.; Mantoura, R. F. C.; Liss, P. S. Ocean-atmosphere exchange and atmospheric speciation of ammonia and methylamines in the region of the NW Arabian Sea. *Global Biogeochem. Cycles* **1999**, *13*, 161−178.

(13) Arévalo-Martínez, D. L.; Steinhoff, T.; Brandt, P.; Körtzinger, A.; Lamont, T.; Rehder, G.; Bange, H. W. N_2O emissions from the northern benguela upwelling system. *Geophys. Res. Lett.* **2019**, *46*, 3317−3326.

(14) Johnson, M. T.; Liss, P. S.; Bell, T. G.; Lesworth, T. J.; Baker, A. R.; Hind, A. J.; Jickells, T. D.; Biswas, K. F.; Woodward, E. M. S.; Gibb, S. W. Field observations of the ocean-atmosphere exchange of ammonia: Fundamental importance of temperature as revealed by a comparison of high and low latitudes. *Global Biogeochem. Cycles* **2008**, *22*, GB1019.

(15) Paulot, F.; Jacob, D. J.; Johnson, M. T.; Bell, T. G.; Baker, A. R.; Keene, W. C.; Lima, I. D.; Doney, S. C.; Stock, C. A. Global oceanic emission of ammonia: Constraints from seawater and atmospheric observations. *Global Biogeochem. Cycles* **2015**, *29*, 1165−1178.

(16) Carpenter, L. J.; Archer, S. D.; Beale, R. Ocean-atmosphere trace gas exchange. *Chem. Soc. Rev.* **2012**, *41*, 6473−6506.

(17) Brimblecombe, P.The Global Sulfur Cycle. *Treatise on Geochemistry*, 2nd ed.; Elsevier: Amsterdam, 2014; pp 559−591.

(18) Sievert, S. M.; Kiene, R. P.; Schulz-Vogt, H. N. The sulfur cycle. *Oceanography* **2007**, *20*, 117−123.

(19) Fowler, D.; Steadman, C. E.; Stevenson, D.; Coyle, M.; Rees, R. M.; Skiba, U. M.; Sutton, M. A.; Cape, J. N.; Dore, A. J.; Vieno, M.; et al. Effects of global change during the 21st century on the nitrogen cycle. *Atmos. Chem. Phys.* **2015**, *15*, 13849−13893.

(20) Sköld, O. Sulfonamides and trimethoprim. *Expert Rev. Anti Infect. Ther.* **2010**, *8*, 1−6.

(21) Anacardio, R.; Mullins, F. G. P.; Hannam, S.; Sheikh, M. S.; O'Shea, K.; Aramini, A.; D'Anniballe, G.; D'Anteo, L.; Ferrari, M. P.; Allegretti, M. Development and validation of an LC−MS/MS method for determination of methanesulfonamide in human urine. *J. Chromatogr. B* **2009**, *877*, 2087−2092.

(22) Zhao, Y.; Truhlar, D. G. The M06 suite of density functionals for main group thermochemistry, thermochemical kinetics, non-covalent interactions, excited states, and transition elements: Two new functionals and systematic testing of four M06-class functionals and 12 other functionals. *Theor. Chem. Acc.* **2008**, *120*, 215−241.

(23) Dunning, T. H., Jr.; Peterson, K. A.; Wilson, A. K. Gaussian basis sets for use in correlated molecular calculations. X. the atoms aluminum through argon revisited. *J. Chem. Phys.* **2001**, *114*, 9244−9253.

(24) Arathala, P.; Musah, R. A. Atmospheric oxidation of propanesulfinic acid initiated by OH radicals: reaction mechanism, energetics, rate coefficients, and atmospheric implications. *ACS Earth Space Chem.* **2021**, *5*, 1498−1510.

(25) Chen, J.; Berndt, T.; Møller, K. H.; Lane, J. R.; Kjaergaard, H. G. Atmospheric fate of the CH_3SOO radical from the CH_3S + O_2 equilibrium. *J. Phys. Chem. A* **2021**, *125*, 8933−8941.

(26) Arathala, P.; Musah, R. A. Oxidation of dipropyl thiosulfinate initiated by Cl radicals in the gas phase: Implications for atmospheric chemistry. *ACS Earth Space Chem.* **2021**, *5*, 2878−2890.

(27) Wilson, A. K.; Dunning, T. H. The HSO−SOH isomers revisited: the effect of tight d functions. *J. Phys. Chem. A* **2004**, *108*, 3129−3133.

(28) Kurtén, T.; Lane, J. R.; Jørgensen, S.; Kjaergaard, H. G. A computational study of the oxidation of SO_2 to SO_3 by gas-phase organic oxidants. *J. Phys. Chem. A* **2011**, *115*, 8669−8681.

(29) Fukui, K. The path of chemical reactions - the IRC approach. *Acc. Chem. Res.* **1981**, *14*, 363−368.

(30) Noga, J.; Bartlett, R. J. The full CCSDT model for molecular electronic structure. *J. Chem. Phys.* **1987**, *86*, 7041−7050.

(31) Frisch, M. J.; Trucks, G. W.; Schlegel, H. B.; Scuseria, G. E.; Robb, M. A.; Cheeseman, J. R.; Scalmani, G.; Barone, V.; Petersson, G. A.; Nakatsuji, H.; et al.*Gaussian 16*, Revision B.01; Gaussian, Inc.: Wallingford, CT, 2016.

(32) Rienstra-Kiracofe, J. C.; Allen, W. D.; Schaefer, H. F. The C_2H_5 + O_2 reaction mechanism: High-level ab Initio characterizations. *J. Phys. Chem. A* **2000**, *104*, 9823−9840.

(33) Miller, S. R.; Schultz, N. E.; Truhlar, D. G.; Leopold, D. G. A study of the ground and excited states of Al_3 and Al_3^-. II. computational analysis of the 488 nm anion photoelectron spectrum and a reconsideration of the Al_3 bond dissociation energy. *J. Chem. Phys.* **2009**, *130*, 024304.

(34) Barnes, I.; Hjorth, J.; Mihalopoulos, N. Dimethyl sulfide and dimethyl sulfoxide and their oxidation in the atmosphere. *Chem. Rev.* **2006**, *106*, 940−975.

(35) Arathala, P.; Musah, R. A. Theoretical studies of the gas-phase reactions of S-methyl methanesulfinothioate (dimethyl thiosulfinate) with OH and Cl radicals: reaction mechanisms, energetics, and kinetics. *J. Phys. Chem. A* **2019**, *123*, 8448−8459.

(36) Lester, M. I.; Pond, B. V.; Anderson, D. T.; Harding, L. B.; Wagner, A. F. Exploring the OH + CO reaction coordinate via infrared spectroscopy of the OH−CO reactant complex. *J. Chem. Phys.* **2000**, *113*, 9889−9892.

(37) Smith, I. W. M.; Ravishankara, A. R. Role of hydrogen-bonded intermediates in the bimolecular reactions of the hydroxyl radical. *J. Phys. Chem. A* **2002**, *106*, 4798−4807.

(38) Alvarez-Idaboy, J. R.; Galano, A.; Bravo-Pérez, G.; Ruiz, M. E. Rate constant dependence on the size of aldehydes in the NO_3 + aldehydes reaction. an explanation via quantum chemical calculations and CTST. *J. Am. Chem. Soc.* **2001**, *123*, 8387−8395.

(39) Alvarez-Idaboy, J. R.; Mora-Diez, N.; Vivier-Bunge, A. A quantum chemical and classical transition state theory explanation of negative activation energies in OH addition to substituted ethenes. *J. Am. Chem. Soc.* **2000**, *122*, 3715−3720.

(40) Uc, V. H.; García-Cruz, I.; Hernández-Laguna, A.; Vivier-Bunge, A. New channels in the reaction mechanism of the atmospheric oxidation of toluene. *J. Phys. Chem. A* **2000**, *104*, 7847−7855.

(41) Parandaman, A.; Tangtartharakul, C. B.; Kumar, M.; Francisco, J. S.; Sinha, A. A computational study investigating the energetics and kinetics of the HNCO + $(CH_3)_2NH$ reaction catalyzed by a single water molecule. *J. Phys. Chem. A* **2017**, *121*, 8465−8473.

(42) Arathala, P.; Musah, R. A. Catalytic effect of water and formic acid on the reaction of carbonyl sulfide with dimethyl amine under tropospheric conditions. *Phys. Chem. Chem. Phys.* **2021**, *23*, 8752−8766.

(43) Jørgensen, S.; Jensen, C.; Kjaergaard, H. G.; Anglada, J. M. The gas-phase reaction of methane sulfonic acid with the hydroxyl radical without and with water vapor. *Phys. Chem. Chem. Phys.* **2013**, *15*, 5140−5150.

(44) Galano, A.; Alvarez-Idaboy, J. R.; Bravo-Pérez, G.; Ruiz-Santoyo, M. E. Gas phase reactions of C_1−C_4 alcohols with the OH radical: A quantum mechanical approach. *Phys. Chem. Chem. Phys.* **2002**, *4*, 4648−4662.

(45) Garrett, B. C.; Truhlar, D. G. Variational transition state theory. Primary kinetic isotope effects for atom transfer reactions. *J. Am. Chem. Soc.* **1980**, *102*, 2559−2570.

(46) Garrett, B. C.; Truhlar, D. G. Criterion of minimum state density in the transition state theory of bimolecular reactions. *J. Chem. Phys.* **1979**, *70*, 1593−1598.

(47) Bao, J. L.; Truhlar, D. G. Variational transition state theory: Theoretical framework and recent developments. *Chem. Soc. Rev.* **2017**, *46*, 7548−7596.

(48) Liu, Y. P.; Lynch, G. C.; Truong, T. N.; Lu, D. H.; Truhlar, D. G.; Garrett, B. C. Molecular modeling of the kinetic isotope effect for the [1,5]-sigmatropic rearrangement of cis-1,3-pentadiene. *J. Am. Chem. Soc.* **1993**, *115*, 2408−2415.

(49) Zheng, J.; Bao, L.; Meana-Pañeda, R.; Zhang, S.; Lynch, G. C.; Corchado, J. C.; Chuang, Y. Y.; Fast, P. L.; Hu, W. P.; Liu, Y. P.; et al.*POLYRATE*, version 2016-2A; University of Minnesota: Minneapolis, MN, 2016.

(50) McQuarrie, D. A.*Statistical Mechanics*; University Science Books: Sausalito, CA, 2000.

(51) Atkinson, R.; Baulch, D. L.; Cox, R. A.; Crowley, J. N.; Hampson, R. F.; Hynes, R. G.; Jenkin, M. E.; Rossi, M. J.; Troe, J. Evaluated kinetic and photochemical data for atmospheric chemistry: Volume I - gas phase reactions of O*x*, HO*x*, NO*x* and SO*x* species. *Atmos. Chem. Phys.* **2004**, *4*, 1461−1738.

(52) Burkholder, J. B.; Sander, S. P.; Abbatt, J.; Barker, J. R.; Huie, R. E.; Kolb, C. E.; Kurylo, M. J.; Orkin, V. L.; Wilmouth, D. M.; Wine, P. H.*Chemical kinetics and photochemical data for use in atmospheric studies*. Evaluation No. 18; JPL Publication 15-10; Jet Propulsion Laboratory: Pasadena, CA, 2015. http://jpldataeval.jpl.nasa.gov.

(53) Arathala, P.; Musah, R. A. Thermochemistry and kinetics of the atmospheric oxidation reactions of propanesulfinyl chloride initiated by OH radicals: A computational approach. *J. Phys. Chem. A* **2022**, *126*, 4264−4276.

(54) Parandaman, A.; Kumar, M.; Francisco, J. S.; Sinha, A. Organic acid formation from the atmospheric oxidation of gem diols: Reaction mechanism, energetics, and rates. *J. Phys. Chem. A* **2018**, *122*, 6266−6276.

(55) Alam, M. A.; Ren, Z.; da Silva, G. Nitramine and nitrosamine formation is a minor pathway in the atmospheric oxidation of methylamine: A theoretical kinetic study of the $CH_3NH + O_2$ reaction. *Int. J. Chem. Kinet.* **2019**, *51*, 723−728.

(56) Orlando, J. J.; Tyndall, G. S. Laboratory studies of organic peroxy radical chemistry: An overview with emphasis on recent issues of atmospheric significance. *Chem. Soc. Rev.* **2012**, *41*, 6294−6317.

(57) Li, S.; Lu, K.; Ma, X.; Yang, X.; Chen, S.; Zhang, Y. Field measurement of the organic peroxy radicals by the low-pressure reactor plus laser-induced fluorescence spectroscopy. *Chin. Chem. Lett.* **2020**, *31*, 2799−2802.

(58) Boyd, A. A.; Flaud, P.-M.; Daugey, N.; Lesclaux, R. Rate constants for $RO_2 + HO_2$ reactions measured under a large excess of HO_2. *J. Phys. Chem. A* **2003**, *107*, 818−821.

(59) Atkinson, R.; Arey, J. Atmospheric degradation of volatile organic compounds. *Chem. Rev.* **2003**, *103*, 4605−4638.

(60) Crounse, J. D.; Nielsen, L. B.; Jørgensen, S.; Kjaergaard, H. G.; Wennberg, P. O. Autoxidation of organic compounds in the atmosphere. *J. Phys. Chem. Lett.* **2013**, *4*, 3513−3520.

(61) Møller, K. H.; Bates, K. H.; Kjaergaard, H. G. The importance of peroxy radical hydrogen-shift reactions in atmospheric isoprene oxidation. *J. Phys. Chem. A* **2019**, *123*, 920−932.

(62) Fu, Z.; Xie, H.-B.; Elm, J.; Liu, Y.; Fu, Z.; Chen, J. Atmospheric autoxidation of organophosphate esters. *Environ. Sci. Technol.* **2022**, *56*, 6944−6955.

(63) Hofzumahaus, A.; Rohrer, F.; Lu, K.; Bohn, B.; Brauers, T.; Chang, C.-C.; Fuchs, H.; Holland, F.; Kita, K.; Kondo, Y.; et al. Amplified trace gas removal in the troposphere. *Science* **2009**, *324*, 1702−1704.

(64) Pagonis, D.; Price, D. J.; Algrim, L. B.; Day, D. A.; Handschy, A. V.; Stark, H.; Miller, S. L.; de Gouw, J.; Jimenez, J. L.; Ziemann, P. J. Time-resolved measurements of indoor chemical emissions, deposition, and reactions in a university art museum. *Environ. Sci. Technol.* **2019**, *53*, 4794−4802.

(65) Lelieveld, J.; Butler, T. M.; Crowley, J. N.; Dillon, T. J.; Fischer, H.; Ganzeveld, L.; Harder, H.; Lawrence, M. G.; Martinez, M.; Taraborrelli, D.; et al. Atmospheric oxidation capacity sustained by a tropical forest. *Nature* **2008**, *452*, 737−740.

(66) Clyne, M. A. A. Reactions of the HNO molecule. *Symp. Combust. Proc.* **1965**, *10*, 311−316.

(67) Arathala, P.; Tangtartharakul, C. B.; Sinha, A. Atmospheric ring-closure and dehydration reactions of 1,4-hydroxycarbonyls in the gas phase: The impact of catalysts. *J. Phys. Chem. A* **2021**, *125*, 5963−5975.

Recommended by ACS

Experimental and Theoretical Kinetic Studies of the Ozonolysis of Selected Allyl Sulfides ($H_2C{=}CHCH_2SR$, R = CH_3, CH_3CH_2): The Effect of Nascent OH Radicals

Alejandro L. Cardona, Mariano Teruel, *et al.*

SEPTEMBER 16, 2022
THE JOURNAL OF PHYSICAL CHEMISTRY A

READ

Theoretical Investigations of the OH-Initialized Oxidation of 4-Methyl-3-Penten-2-One in the Atmosphere

Benni Du and Weichao Zhang

AUGUST 26, 2022
ACS EARTH AND SPACE CHEMISTRY

READ

Important Routes for Methanediol Formation by Formaldehyde Hydrolysis Catalyzed by Iodic Acid and for the Contribution to an Iodic Acid Sink by the Reaction of...

Na Lin, Bo Long, *et al.*

JUNE 22, 2022
ACS EARTH AND SPACE CHEMISTRY

READ

Quantum Chemical and Chemical Kinetic Investigation on Hydrogen Abstraction Reactions of $CF_3CF_2C(O)OCH_3$ and $CHF_2CF_2C(O)OCH_3$ with OH Radicals and Fate of Halo...

Kanika Guleria and Ranga Subramanian

MAY 13, 2022
ACS EARTH AND SPACE CHEMISTRY

READ

Get More Suggestions >